JM PAPERS

Mode coupling between two different interfaces of a gas layer subject to a shock

Chenren Chen[1], He Wang[1], Zhigang Zhai[1],† and Xisheng Luo[1,2],†

[1]Advanced Propulsion Laboratory, Department of Modern Mechanics, University of Science and Technology of China, Hefei 230026, PR China

[2]State Key Laboratory of High Temperature Gas Dynamics, Institute of Mechanics, Chinese Academy of Sciences, Beijing 100190, PR China

Shock-tube experiments and theoretical studies have been performed to highlight mode-coupling in an air–SF_6–air fluid layer. Initially, the two interfaces of the layer are designed as single mode with different basic modes. It is found that as the two perturbed interfaces become closer, interface coupling induces a different mode from the basic mode on each interface. Then mode coupling further generates new modes. Based on the linear model (Jacobs *et al.*, *J. Fluid Mech.*, vol. 295, 1995, pp. 23–42), a modified model is established by considering the different accelerations of two interfaces and the waves' effects in the layer, and provides good predictions to the linear growth rates of the basic modes and the modes generated by interface coupling. It is observed that interface coupling behaves differently to the nonlinear growth of the basic modes, which can be characterized generally by the existing or modified nonlinear model. Moreover, a new modal model is established to quantify the mode-coupling effect in the layer. The mode-coupling effect on the amplitude growth is negligible for the basic modes, but is significant for the interface-coupling modes when the initial wavenumber of one interface is twice the wavenumber of the other interface. Finally, amplitude freeze-out of the second single-mode interface is achieved theoretically and experimentally through interface coupling. These findings may be helpful for designing the target in inertial confinement fusion to suppress the hydrodynamic instabilities.

Key words: shock waves

1. Introduction

Richtmyer–Meshkov (RM) instability occurs when a perturbed interface separating two different fluids is impacted by a shock wave (Richtmyer 1960; Meshkov 1969).

† Email addresses for correspondence: sanjing@ustc.edu.cn, xluo@ustc.edu.cn

The development of the RM instability is driven mainly by baroclinic vorticity produced by misalignment of the pressure and density gradients. The RM instability plays essential roles in many applications, such as inertial confinement fusion (ICF) (Lindl *et al.* 2014; Qiao & Lan 2021; Zhou *et al.* 2021), supersonic combustion (Yang, Kubota & Zukoski 1993) and supernova explosions (Kuranz *et al.* 2018). Over the past decades, several reviews have been published to conclude the achievements in the RM instability study (Zabusky 1999; Brouillette 2002; Ranjan, Oakley & Bonazza 2011; Zhou 2017*a*,*b*; Zhai *et al.* 2018).

For an initial single-mode interface, mode coupling can be ignored until the harmonics grow significantly (Zhou 2017*a*; Liu *et al.* 2018*a*). A perturbation expansion model with fourth-order accuracy (ZS model) was developed by Zhang & Sohn (1997) to calculate the amplitudes of high-order harmonics. The perturbation expansion method was further simplified by Vandenboomgaerde, Gauthier & Mügler (2002) to obtain higher-order expressions of the harmonics than that in the ZS model. When the initial perturbation is multi-mode, the different basic modes interact with each other, and mode coupling causes the generation of new modes at the early stage (Brouillette 2002; Zhou 2017*b*). Mode coupling for a multi-mode interface has been investigated widely (Rikanati, Alon & Shvarts 1998; Di Stefano *et al.* 2015; McFarland *et al.* 2015; Mohaghar *et al.* 2019). Theoretically, Haan (1991) proposed a modal model (Haan model) with second-order accuracy to quantify the mode-coupling effect on the Rayleigh–Taylor (RT) instability development (Rayleigh 1883; Taylor 1950). Then the applicability range of the Haan model was extended by Ofer *et al.* (1996). These two models were reformulated recently to apply them to the multi-mode RM instability (Liang *et al.* 2021). Experimentally, the mode coupling on a single-interface development has been explored extensively through shock-tube experiments (Luo *et al.* 2020; Liang *et al.* 2021; Xu *et al.* 2023), and several models have been verified.

In many applications, the RM instability grows on the interfaces of a fluid layer. For example, the RM instability in ICF occurs on both the ablator front and the interface between the ablator and deuterium–tritium ice (Betti & Hurricane 2016; Qiao & Lan 2021). For the RM instability of a fluid layer, most previous studies considered the perturbation of only one mode, i.e. both single-mode interfaces of the fluid layer have the same mode (Jacobs *et al.* 1995; Mikaelian 1995; Liang & Luo 2021). Theoretically, a linear analytic theory for the RM instability in a perturbed fluid layer with only one wavenumber was first proposed by Mikaelian (1985, 1995), and later verified by numerical simulations (Mikaelian 1996). Through solving velocity potential functions of a heavy layer, Jacobs *et al.* (1995) deduced a linear model (the J-model hereafter) for predicting the perturbation growth rates of both interfaces, and a vortex model for predicting the width growth of the fluid layer. The J-model was modified by Liang & Luo (2021) to predict the perturbation linear growth rates of a heavy layer. Recently, the effect of the finite thickness of two superimposed fluids on harmonics in the RM instability for arbitrary Atwood numbers was also investigated (Liu *et al.* 2018*b*). Experimentally, the gas curtain technique was used by Jacobs *et al.* (1993) to produce a thin SF_6 layer in air, and the shocked layer evolution was investigated. Based on the gas curtain technique, the width of the shocked gas layer was measured (Jacobs *et al.* 1995), and the circulation in the curtain was calculated (Prestridge *et al.* 2000) to verify the vortex model. Recently, the soap-film technique was used widely in creating a gas layer, and extensive studies have been conducted (Liang & Luo 2021, 2023*a*,*b*; Zhang *et al.* 2023), focusing on the effects of initial amplitude, width of the gas layer, and perturbation phase on a fluid layer development. When the two interfaces of a fluid layer have the same mode, mode coupling is absent until nonlinearity is significant
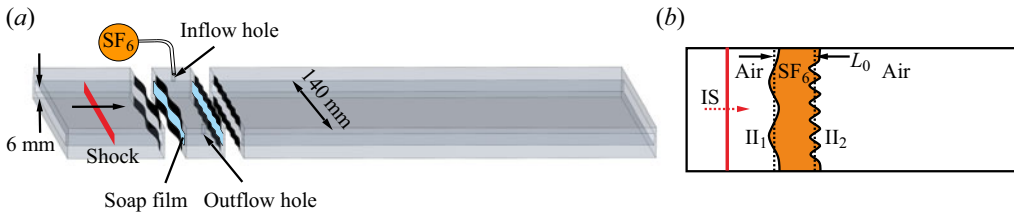
Figure 1. Schematics of (*a*) the soap-film interface generation, and (*b*) the initial interface configuration studied. Here, IS is the incident shock, II_1 is the first interface (air–SF$_6$), II_2 is the second interface (SF$_6$–air), and L_0 is the initial width of the SF$_6$ layer.

(Liang & Luo 2021; Liang 2022). In real scenarios, however, the interfaces of the fluid layer often have different basic modes. The previous work always considered coupling between modes on the same interface: whether and how the modes on the different interfaces couple; and how to quantify mode coupling between different interfaces. Due to difficulties in forming such a fluid layer with the specific modes on interfaces in experiments and more complicated mechanisms involved, the related studies are rare and these questions remain unclear.

In this work, the soap-film technique is used to create the fluid layer, in which two different modes are present on the two initial interfaces. Seven kinds of disturbed SF$_6$ gas layer with different mode combinations are considered. Through one-dimensional theory and experiments on the undisturbed layer, the wave patterns and the concentration of SF$_6$ inside the layer are obtained. The existing linear and nonlinear models are modified to describe the perturbation evolution of basic modes, and a new modal model is established to quantify the mode-coupling effect. Finally, freeze-out of the amplitude growth of the second single-mode interface is discussed.

2. Experimental methods

The soap-film technique (Liu *et al.* 2018*a*; Liang *et al.* 2021) is used to generate the well-defined discontinuous interfaces of the fluid layer. As shown in figure 1(*a*), there are three devices, with width 140 mm and height 6 mm. The soap-film interfaces are first generated at both sides of the middle device. Then SF$_6$ is pumped into the middle device through the inflow hole, and air is discharged through the outflow hole. Once the SF$_6$ concentration satisfies the requirement, the inflation stops. Then the three devices are connected, and an SF$_6$ gas layer with two interfaces is formed. For different runs, the inflation rate and duration are the same to ensure a similar concentration of SF$_6$ in the gas layer as far as possible. The concentration of SF$_6$ is determined by comparing the velocities of the incident shock and transmitted shock, and the interface velocity jump, measured from experiments with those predicted by one-dimensional theory.

The schematic of the initial interface configuration is shown in figure 1(*b*). The two single-mode interfaces with different wavenumbers are considered. Seven kinds of fluid layer with different wavenumber combinations and relative phase, as shown in table 1, are studied. In this work, the initial phase of the perturbation on the second interface (II_2) is defined as positive. In the first six cases, the phase of the first interface (II_1) is positive, while the phase of II_1 in the seventh case is negative. A dimensionless number $K = k_1/k_2$ (where k_1 and k_2 are the wavenumbers of II_1 and II_2) is defined to represent different mode-coupling effects. Here, $k_1 a_1^-$ and $k_2 a_2^-$ (where a_1^- and a_2^- are the initial amplitudes of II_1 and II_2, respectively) are all close to 0.1, and the tiny differences among

984 A38-3

Case	λ_1 (mm)	λ_2 (mm)	K	$k_1 a_1^-$	$k_2 a_2^-$
20-60-IP	20	60	3	0.083	0.098
30-60-IP	30	60	2	0.091	0.098
20-30-IP	20	30	1.5	0.083	0.092
30-20-IP	30	20	1/1.5	0.092	0.083
40-20-IP	40	20	1/2	0.095	0.083
60-20-IP	60	20	1/3	0.098	0.083
60-20-AP	60	20	1/3	−0.098	0.083

Table 1. Interface parameters of perturbed cases: λ_1 and λ_2 (k_1 and k_2, a_1^- and a_2^-) are the wavelengths (wavenumbers, initial amplitudes) of II_1 and II_2, respectively, and $K = k_1/k_2$. Here, 'IP' ('AP') means the perturbations on the two interfaces have the same (opposite) phase.

cases are caused by three-dimensionality of the soap-film interface (Wang *et al.* 2022). To highlight the mode-coupling and interface-coupling effects, the initial width of the gas layer (L_0, defined as the distance between the balanced positions of two interfaces) is fixed as 20 mm. The choice of L_0 makes the interface-coupling effect strong enough but avoids the coalescing of two interfaces (Liang & Luo 2021).

The experiments are conducted in a shock tube (Liu *et al.* 2018*a*; Guo *et al.* 2022), and the incident shock Mach number is 1.31 ± 0.01. The flow field is recorded by high-speed schlieren photography. The frame rate of the camera (FASTCAM SA-Z, Photron Ltd) is 50 400 frames per second, and the exposure time is $0.78\,\mu s$. The spatial resolution is $\sim 0.26\,mm\,pixel^{-1}$. The ambient pressure and temperature are $101.3 \pm 0.1\,kPa$ and $295 \pm 1.5\,K$, respectively. At least three successful experimental runs are performed for each case to ensure the experimental repeatability. The boundary layer effect has already been discussed (Liu *et al.* 2018*a*), and is ignored here.

3. Results and discussion

3.1. *Undisturbed layer*

The schlieren images of the undisturbed SF_6 layer after the shock impact are presented in figure 2(*a*). The initial time is defined as the moment when the incident shock (IS) meets the average position of the first initial interface (II_1). After IS impacts II_1, the first transmitted shock wave (TS_1) moving downstream in SF_6, the reflected shock (RS) moving upstream in air, and a shocked air–SF_6 interface (SI_1) are formed (39 μs). Then TS_1 impacts the second initial interface (II_2), which produces a shocked SF_6–air interface (SI_2), the second transmitted shock wave (TS_2) moving downstream in air (277 μs), and reflected rarefaction waves (RW) moving upstream in SF_6. These RW will interact with SI_1, reflecting compression waves (CW) that subsequently interact with SI_2. Both RW and CW cannot be observed in the schlieren images of our experiments due to their weak intensity. As studied by Liang & Luo (2021), RW and CW significantly affect the movements of SI_1 and SI_2, respectively. During the experimental time studied, after CW interact with SI_2, the two undisturbed interfaces move parallel, and no obvious disturbances are generated on the interfaces.

The trajectories of shock waves and interfaces extracted from experiment and predicted by one-dimensional theory are compared in figure 2(*b*), and their velocities are provided in table 2. After CW impact SI_2, the two shocked interfaces move steadily, and the effects of other reflected waves can be ignored. Due to the similar initial conditions for
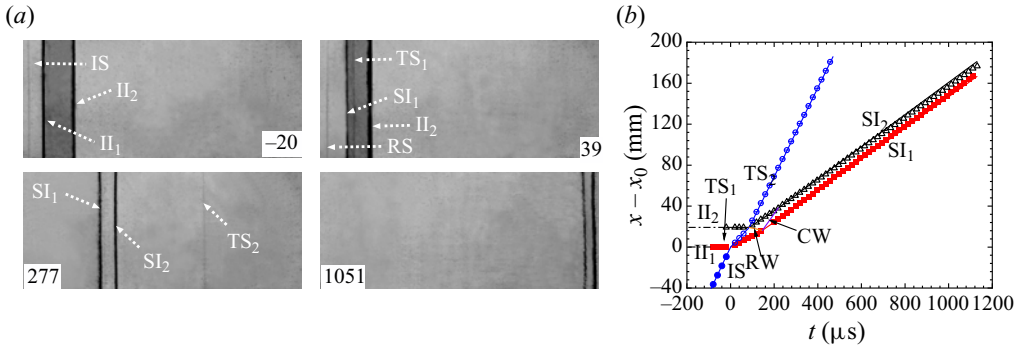
Figure 2. (*a*) Schlieren images of a planar SF_6 layer accelerated by a planar shock, and (*b*) the trajectories of the interfaces and waves. Here, II_1 and II_2 (SI_1 and SI_2) are the first and second initial (shocked) interfaces respectively; TS_1 and TS_2 are the transmitted shock waves in SF_6 and in air, respectively; RS is the reflected shock; RW is reflected rarefaction waves; CW is compression waves; and x_0 is the initial position of II_1.

M_s	Δu_1	Δu_2	Δu_R	Δu_C	v_1	v_2	t_1	t_R	t_C	c_1	c_2
1.31	111.2	142.6	41.7	14.5	453.1	226.2	85.9	146.2	219.4	160.9	158.3

Table 2. Theoretical parameters in undisturbed case: M_s is the Mach number of IS; Δu_1, Δu_2, Δu_R and Δu_C are the jump velocities of II_1 induced by IS, II_2 induced by TS_1, II_1 induced by RW, and II_2 induced by CW, respectively; v_1 and v_2 are the velocities of IS and TS_1, respectively; t_1, t_R and t_C denote the times when TS_1 impacts II_2, RW impact SI_1, and CW impact SI_2, respectively; c_1 (c_2) is the sound speed of the gas between SI_1 and the RW front (between SI_2 and the RW tail). The units of velocity and time are $m\,s^{-1}$ and μs.

different cases, the parameters in table 2 are considered as the initial parameters in the following experiments. In this work, the volume fraction of SF_6 in the gas layer is 75 %. The Atwood numbers of pre-shock (A^-) and post-shock (A^+) SF_6 layer (A is defined as $(\rho_1 - \rho_2)/(\rho_1 + \rho_2)$, with ρ_1 and ρ_2 being the densities of gases inside and outside the layer, respectively) equal 0.60 and 0.64, respectively. Here, three specific times are defined to facilitate subsequent calculations: t_1 denotes the time when TS_1 impacts II_2 and RW are initially generated at $t = t_1$; t_R and t_C denote the times when RW meet SI_1 and CW meet SI_2, respectively. Here, t_1, t_R and t_C can be calculated as

$$\left.\begin{aligned}
t_1 &= \frac{L_0}{v_2}, \\
t_R &= t_1 + \frac{L_0\left(1 - \dfrac{\Delta u_1}{v_2}\right)}{c_1}, \\
t_C &= t_R + \frac{L_0\left(1 - \dfrac{\Delta u_1}{v_2}\right)\left(1 + \dfrac{\Delta u_2 - \Delta u_1}{c_1}\right)}{c_2},
\end{aligned}\right\} \tag{3.1}$$

where v_2 is the velocity of TS_1, Δu_1 and Δu_2 are the jump velocities of II_1 and II_2 induced by shocks, respectively, c_1 is the sound speed of the gas between SI_1 and the RW front, and c_2 is the sound speed of the gas between SI_2 and the RW tail.

3.2. *Perturbed layers*

3.2.1. *Interface morphology*

Schlieren images of the developments of the shock-impacted fluid layer for seven cases are shown in figure 3. The wave–interface interaction processes are similar to those in the undisturbed case, and the relevant descriptions are omitted here. Taking case 30-20-IP as an example, when CW impact SI_2, the phase inversion process of the perturbation on SI_2 has been completed, and TS_2 is away from SI_2 (298 μs). Just after CW impact SI_2, the perturbations on two interfaces can still be considered as single mode. Later, the multi-mode perturbations grow on SI_1 and SI_2 (695 μs). Finally, spikes and bubbles arise symmetrically (1091 μs). The sizes and shapes of the bubble and spike on SI_1 and SI_2 differ significantly. From the schlieren images, the interface profile is clear enough to extract its contour, and can still be described as a single-valued function so that the fast Fourier transform can be applied to obtain the amplitude of each mode (Liu *et al.* 2018*a*). The evolutions of the bubbles and spikes at the two interfaces are very sensitive to the value of K. When the first interface is disturbed at a higher mode than the second interface ($K > 1$), the perturbation on SI_2 remains a quasi-single-mode profile, and the bubbles and spikes develop without inclination. However, the multi-mode perturbations on SI_1 appear more significant than those on SI_2, and the bubbles and spikes on SI_1 develop asymmetrically. Specifically, in case 20-60-IP, the middle bubble on SI_1 has a wider spread but a smaller amplitude than the side bubbles, and the spikes on SI_1 develop with an apparent inclination to the middle bubble. In case 30-60-IP, the middle spike has a greater scale than the side spikes, and the bubbles are inclined to the side spikes. Besides, vortices have already arisen on the side spikes, which indicate that nonlinearity occurs earlier on the side spike than the middle spike. In case 20-30-IP, the middle bubble has a narrower spread but a larger amplitude than the side bubbles, and the spikes are also inclined to the middle bubble. On the whole, if the bubble (spike) on SI_1 faces directly the spike (bubble) on SI_2, then it is deformed weakly. Otherwise, the bubble (spike) on SI_1 deforms greatly. When $K < 1$, the first interface has a lower mode disturbance than the second one, and the multi-mode perturbations on SI_2 appear more significant compared with those on SI_1. In case 30-20-IP, the middle bubble on SI_1 has a larger amplitude than the side bubbles, and two spikes develop equally, with a flattened head. The middle spike on SI_2 has a larger amplitude and a narrower head compared with the side spikes, and two bubbles develop similarly. In cases 40-20-IP and 60-20-IP, a small middle spike on SI_2 occurs, and the shape of the side spikes on SI_2 is similar to the shape of the side bubbles on SI_1. For these two cases, the bubbles on SI_1 behave quite differently, which illustrates the importance of the wavenumber combination. In case 60-20-AP, in contrast, small side spikes occur on SI_2. In general, the shape of SI_1 is still dominated by its initial basic mode, while the shape of SI_2 obviously presents multi-mode.

3.2.2. *Linear growth of amplitude*

Previous works (Jacobs *et al.* 1995; Mikaelian 1996) have revealed that the amplitudes of a shocked heavy layer grow linearly after the compression stage and start-up process. Considering a planar fluid layer (with thickness L) that is composed of a fluid of density ρ_1 being surrounded by a fluid of density ρ_2, Jacobs *et al.* (1995) proposed the J-model to predict the perturbation growth rates of the shocked two interfaces. When the fluids are incompressible and irrotational, the equations that govern the growth of infinitesimal disturbances on the interfaces of the layer can be expressed as
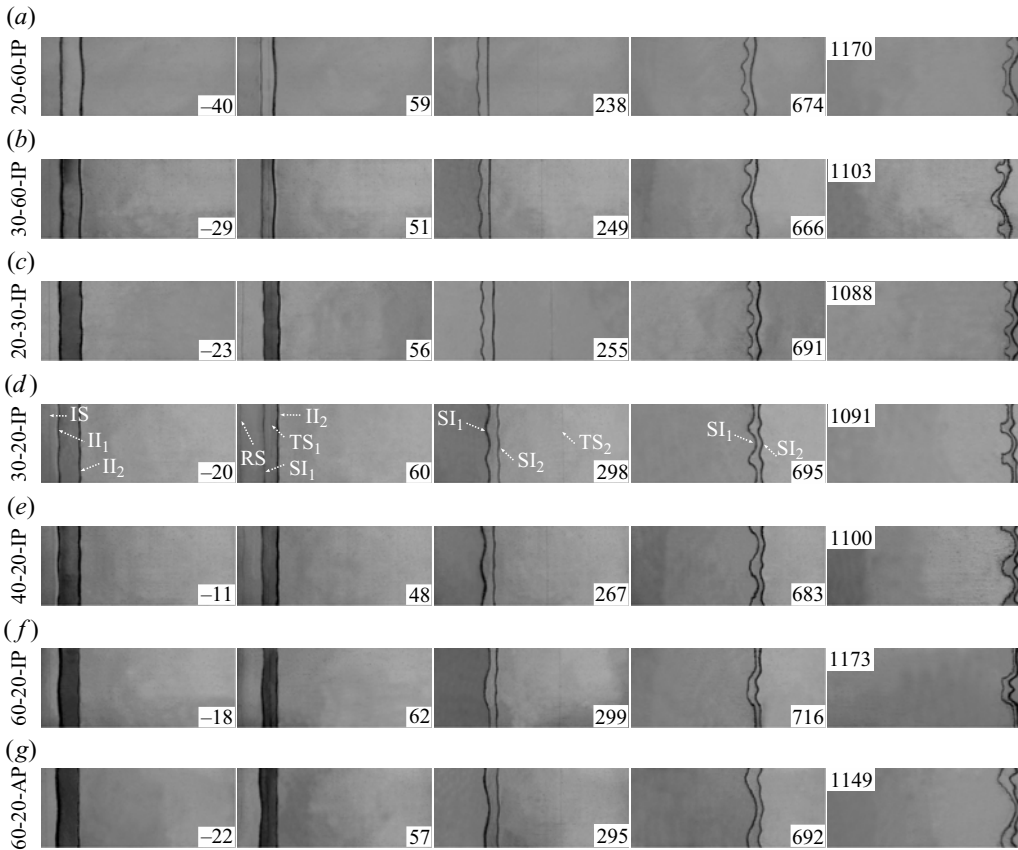
$$\nabla^2\phi = 0, \tag{3.2}$$

Figure 3. Schlieren images of the shock-induced fluid layer evolution for different cases. The symbols have the same meanings as in figure 2. Numbers denote time in μs.

where ϕ is the velocity potential of the fluid, and the kinematic and pressure conditions on the interfaces are

$$\left.\begin{array}{l} \dfrac{\partial \eta}{\partial t} - \dfrac{\partial \phi}{\partial y} = 0, \\[2mm] \rho\, \dfrac{\partial \phi}{\partial t} - \rho g \eta + p = P_0. \end{array}\right\} \tag{3.3}$$

Here, p is the pressure, g is the acceleration, η is the perturbation shape on the interfaces, and P_0 is a constant equalling the pressure at the interface in the unperturbed rest state.

As shown in figure 4, the periodic perturbations set in the layer are of the form

$$\left.\begin{array}{l} \eta_1 = a_1(t)\cos(kx), \\[1mm] \eta_2 = a_2(t)\cos(kx), \end{array}\right\} \tag{3.4}$$
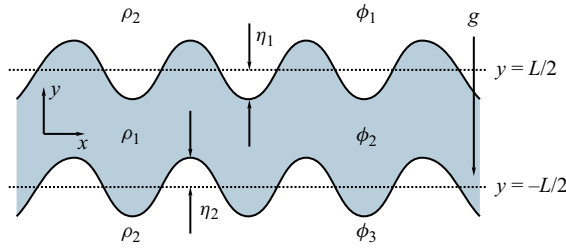
Figure 4. Schematic showing the configuration analysed using linear stability theory for the double-interface system, where ρ_1 and ρ_2 are the densities of the fluids inside and outside the layer, respectively, η_1 and η_2 represent the perturbation shapes of the two interfaces, ϕ_1, ϕ_2 and ϕ_3 are the velocity potentials, L is the initial layer thickness, and g is the acceleration of the two interfaces.

where $a_1(t)$ and $a_2(t)$ are the amplitudes of the first and second interfaces, respectively. Then the velocity potentials in the three fluids can be obtained and expressed as

$$\left.\begin{aligned} \phi_1 &= b_1(t)\,e^{-k(y-L/2)}\cos(kx), \\ \phi_2 &= -\left[\frac{b_1 + b_2}{2}\frac{\sinh(ky)}{\cosh(kL/2)} + \frac{b_1 - b_2}{2}\frac{\cosh(ky)}{\sinh(kL/2)}\right]\cos(kx), \\ \phi_3 &= -b_2(t)\,e^{k(y+L/2)}\cos(kx), \end{aligned}\right\} \quad (3.5)$$

where b_1 and b_2 are the functions of time in the velocity potentials. Substituting (3.4) and (3.5) into (3.3) and (3.2), the J-model (Jacobs *et al.* 1995) can then be deduced as

$$\left.\begin{aligned} \frac{d^2 a_1}{dt^2} + \frac{d^2 a_2}{dt^2} &= kA_t g(a_1 - a_2), \\ \frac{d^2 a_1}{dt^2} - \frac{d^2 a_2}{dt^2} &= kA_c g(a_1 + a_2), \end{aligned}\right\} \quad (3.6)$$

where

$$\left.\begin{aligned} A_t &= \frac{\rho_1 - \rho_2}{\rho_1 \tanh(kL/2) + \rho_2}, \\ A_c &= \frac{\rho_1 - \rho_2}{\rho_1 \coth(kL/2) + \rho_2}, \end{aligned}\right\} \quad (3.7)$$

are the two modified Atwood numbers.

In this work, $\rho_1 = 7.98\ \text{kg m}^{-3}$ ($\rho_2 = 1.78\ \text{kg m}^{-3}$) is the fluid density inside (outside) the layer after the reflected compression waves in the layer (CW) interact with the shocked second interface (SI$_2$). Here, L is chosen as the distance between the two shocked interfaces (SI$_1$ and SI$_2$) after CW collide with SI$_2$, and can be expressed as

$$L = L_0\left(1 - \frac{\Delta u_1}{v_2}\right)\left(1 + \frac{\Delta u_2 - \Delta u_1}{c_1}\right)\left(1 - \frac{\Delta u_1 + \Delta u_R - \Delta u_2}{c_2}\right), \quad (3.8)$$

where Δu_R is the jump velocity of SI$_1$ induced by the reflected rarefaction waves in the layer (RW). In previous work (Jacobs *et al.* 1995; Liang & Luo 2021), the accelerations g of two interfaces of the layer were considered the same for both RT and RM instabilities. However, when a shock encounters a gas layer with a finite thickness, the accelerations of the two interfaces are different. Assuming that g_1 and g_2 represent the accelerations of the

984 A38-8

first and second interfaces, respectively, and then substituting (3.4) and (3.5) into (3.3) and (3.2), yields

$$
\left.\begin{aligned}
\frac{\mathrm{d}a_1}{\mathrm{d}t} &= -kb_1, \\
\frac{\mathrm{d}a_2}{\mathrm{d}t} &= -kb_2,
\end{aligned}\right\}
\tag{3.9}
$$

$$
\left.\begin{aligned}
\frac{\mathrm{d}b_1}{\mathrm{d}t} + \frac{\mathrm{d}b_2}{\mathrm{d}t} &= -A_t(g_1 a_1 - g_2 a_2), \\
\frac{\mathrm{d}b_1}{\mathrm{d}t} - \frac{\mathrm{d}b_2}{\mathrm{d}t} &= -A_c(g_1 a_1 + g_2 a_2).
\end{aligned}\right\}
\tag{3.10}
$$

Combining (3.9) with (3.10), the J-model can be rewritten as

$$
\left.\begin{aligned}
\frac{\mathrm{d}^2 a_1}{\mathrm{d}t^2} + \frac{\mathrm{d}^2 a_2}{\mathrm{d}t^2} &= kA_t(g_1 a_1 - g_2 a_2), \\
\frac{\mathrm{d}^2 a_1}{\mathrm{d}t^2} - \frac{\mathrm{d}^2 a_2}{\mathrm{d}t^2} &= kA_c(g_1 a_1 + g_2 a_2).
\end{aligned}\right\}
\tag{3.11}
$$

For the RM instability in this work, based on the experimental movements of the undisturbed interfaces shown in figure 2, the two interfaces in the layer will, respectively, experience two acceleration processes. For the first interface, the jump velocities induced by the incident shock (IS) and the rarefaction waves (RW) are Δu_1 and Δu_R, respectively. For the second interface, the jump velocities induced by the transmitted shock (TS_1) and the compression waves (CW) are Δu_2 and Δu_C, respectively. Due to the very short durations of the waves interacting with the interfaces, the Dirac δ-function is always used to model the shock impacting the gas layer (Jacobs *et al.* 1995; Liang & Luo 2023*a*). Therefore, the accelerations g_1 and g_2 can be expressed as

$$
\left.\begin{aligned}
g_1 &= \Delta u_1\,\delta t + \Delta u_R\,\delta(t - t_R), \\
g_2 &= \Delta u_2\,\delta(t - t_1) + \Delta u_C\,\delta(t - t_C),
\end{aligned}\right\}
\tag{3.12}
$$

where t_1, t_R and t_C have been defined in (3.1). Substituting (3.12) into (3.11) and integrating the equation, a new model for predicting the linear growth rate of the heavy layer after CW impact SI_2 is established:

$$
\left.\begin{aligned}
\frac{\mathrm{d}a_1}{\mathrm{d}t} + \frac{\mathrm{d}a_2}{\mathrm{d}t} &= kA_t(\Delta u_1\,a_1^+ + \Delta u_R\,a_1^R - \Delta u_2\,a_2^0 - \Delta u_C\,a_2^C), \\
\frac{\mathrm{d}a_1}{\mathrm{d}t} - \frac{\mathrm{d}a_2}{\mathrm{d}t} &= kA_c(\Delta u_1\,a_1^+ + \Delta u_R\,a_1^R + \Delta u_2\,a_2^0 + \Delta u_C\,a_2^C).
\end{aligned}\right\}
\tag{3.13}
$$

According to the impulsive model (Richtmyer 1960) and MB model (Meyer & Blewett 1972), in (3.13), a_1^+ is the amplitude of SI_1 just after being impacted by IS; a_1^R is the amplitude of SI_1 just after being impacted by RW; a_2^0 is the average amplitude of the unshocked and shocked second interface; and a_2^C is the average amplitude of SI_2 before and after being impacted by CW.

Note that (3.13) is established assuming that both interfaces have the same wavenumber. In the linear regime, no additional modes except the initial basic mode are generated even if interface coupling is present. In this work, due to the different initial perturbation wavenumbers on two interfaces (k_1 and k_2 for the first and second initial interfaces,
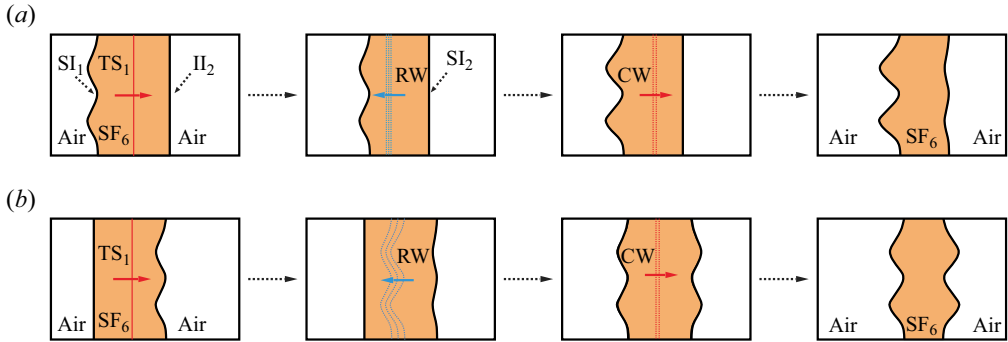
(a)

(b)

Figure 5. Sketches of the interactions of TS_1 with II_1, RW with SI_1, and CW with SI_2: (a) II_2 is planar and II_1 is perturbed; (b) II_1 is planar and II_2 is perturbed.

respectively), the perturbation with k_1 (k_2) will be imprinted on SI_2 (SI_1) through such as interface coupling. In other words, both perturbation modes are present on SI_2 and SI_1 even in the linear regime. Therefore, it is necessary to predict the linear growth rate of k_1 on SI_2 (k_2 on SI_1). Because mode coupling in the linear regime is weak (Luo *et al.* 2020), we attempt to establish a linear model by considering separately the perturbation growth of k_1 and k_2 on SI_1 (SI_2).

We first consider the perturbation growths of k_1 on SI_1 and SI_2. As sketched in figure 5(a), a single-mode perturbation with k_1 is imposed on II_1 and there is no perturbation on II_2. Because the jump velocities of the interfaces have been calculated as shown in table 2, here the amplitudes of the two interfaces at the specific times are provided to solve (3.13). After IS interacts with II_1, the amplitude of SI_1 (a_1^+) can be expressed as

$$a_1^+ = a_1^- Z_1, \tag{3.14}$$

where a_1^- and $Z_1 = 1 - \Delta u_1/v_1$ are the initial amplitude of II_1 and the compression factor of IS, respectively, and v_1 is the velocity of IS. In previous work (Ishizaki & Nishihara 1997), after a shock interacts with a single-mode interface in the plane geometry, the transmitted shock will be seeded by the initial interface shape. If the initial amplitude of the interface is small, then the transmitted shock has a sinusoidal shape, but its amplitude decreases very quickly because of the pressure perturbation. If the initial amplitude of the interface is high, then the triple-shock configuration will be formed on the transmitted shock front, which is no longer a smooth one (Rikanati *et al.* 2003; Wang *et al.* 2023). The duration of such a transmitted shock recovering to planar will be longer. In the present work, due to the small amplitude of the initial first interface, the amplitude of the transmitted shock when it is generated in the layer (TS_1) is also small. It is believed that TS_1 will recover quickly to almost planar when it interacts with the second interface. As a result, SI_2 is still undisturbed ($a_2^0 = 0$), and planar RW aregenerated.

The planar RW move upstream and interact with SI_1. Due to the stretching of RW, the perturbation amplitude of SI_1 (a_1^R) increases and is of the form

$$a_1^R = a_1^+ R, \tag{3.15}$$

where $R = 1 + \Delta u_R/(c_1 + c_2)$ is the stretching factor of RW. After RW collide with SI_1, CW are reflected and move to SI_2. Similar to TS_1, the amplitude of CW is also ignored in this work when CW encounter the planar SI_2 ($a_2^C = 0$). In other words, considering a

984 A38-10

disturbed Π_1 and a planar Π_2 as shown in figure 5(*a*), because the amplitudes of both TS_1 and CW are ignored in this work, both TS_1 and CW will not seed the perturbation to the second interface, and SI_2 obtains the perturbation only through interface coupling. The specific amplitudes calculated are substituted into (3.13), and the linear growth rates of the perturbations with k_1 (the wavenumber of the initial first interface) on SI_1 and SI_2 can be obtained as

$$\left.\begin{aligned}
\frac{\mathrm{d}a_1}{\mathrm{d}t} &= \frac{k_1[A_t(\Delta u_1\,a_1^+ + \Delta u_R\,a_1^R) + A_c(\Delta u_1\,a_1^+ + \Delta u_R\,a_1^R)]}{2}, \\
\frac{\mathrm{d}a_2}{\mathrm{d}t} &= \frac{k_1[A_t(\Delta u_1\,a_1^+ + \Delta u_R\,a_1^R) - A_c(\Delta u_1\,a_1^+ + \Delta u_R\,a_1^R)]}{2}.
\end{aligned}\right\} \tag{3.16}$$

Figure 6 presents the amplitude developments of k_1 on SI_1 and SI_2 for $K > 1$ (figures 6*a,b*) and $K < 1$ (figures 6*c,d*). Note that the initial time ($t = 0$) here is defined as the moment when the linear growth of perturbation starts (after CW compress SI_2), which is different from the definition earlier. On SI_1, the amplitude of k_1 grows fast, and nonlinearity decreases the amplitude growth rate soon. The model can predict the linear growth of the amplitude of k_1 on SI_1. The slight differences of the linear growth rates among cases are probably ascribed to the slight differences of the initial amplitudes and weak dependence upon k_1, as indicated in figure 7. On SI_2, due to the small initial amplitude of k_1, nonlinearity is weak and the linear model is sufficiently accurate to predict the amplitude evolution, except in cases 30-60-IP and 40-20-IP. In these two cases, the amplitudes of k_1 on SI_2 at late stages are promoted, as shown in figures 6(*b,d*), mainly because of mode coupling, i.e. the self-coupling of k_2 in case 30-60-IP generates k_1, and the mutual coupling of k_2 with k_1 in case 40-20-IP generates k_1. Besides, the linear growth rates of k_1 on SI_2 differ significantly between cases with different k_1, because they are strongly associated with k_1, as indicated in figure 7. Specifically, the linear growth rate of k_1 on SI_2 is greater for a smaller k_1. Relatively, the amplitude of k_1 on SI_2 is small (large) for $K > 1$ ($K < 1$).

If a single-mode perturbation with k_2 is imposed on Π_2, while keeping Π_1 planar ($a_1^+ = 0$), then the results will be different. As shown in figure 5(*b*), because both IS and Π_1 are planar, TS_1 is also planar. Induced by TS_1, the average amplitude of Π_2 and SI_2 just being shocked (a_2^0) can be calculated:

$$a_2^0 = a_2^- (1 + Z_2)/2, \tag{3.17}$$

where a_2^- is the amplitude of Π_2, v_2 is the velocity of TS_1, and $Z_2 = 1 - \Delta u_2/v_2$ is the compression factor of TS_1. The amplitude of SI_2 reduces until phase inversion is finished.

The interaction of TS_1 with Π_2 generates perturbed RW. Note that the amplitude of RW increases with time (Velikovich & Phillips 1996). The amplitude of the RW tail before it impacts SI_1 (a_{RW}) can be calculated by the model proposed by Velikovich & Phillips (1996):

$$a_{RW} = a_2^- Z_2 + k_2 a_2^- c_1 u_r(t_R - t_1), \tag{3.18}$$

where $u_r = \sqrt{(\gamma + 1)(1 - c_2/c_1)/(\gamma - 1)}$ is a factor of RW, and γ is the adiabatic exponent of the gas before the RW front. The time and velocity parameters are all presented in table 2. Due to the RW stretching, the perturbation with k_2 arises on SI_1 just being
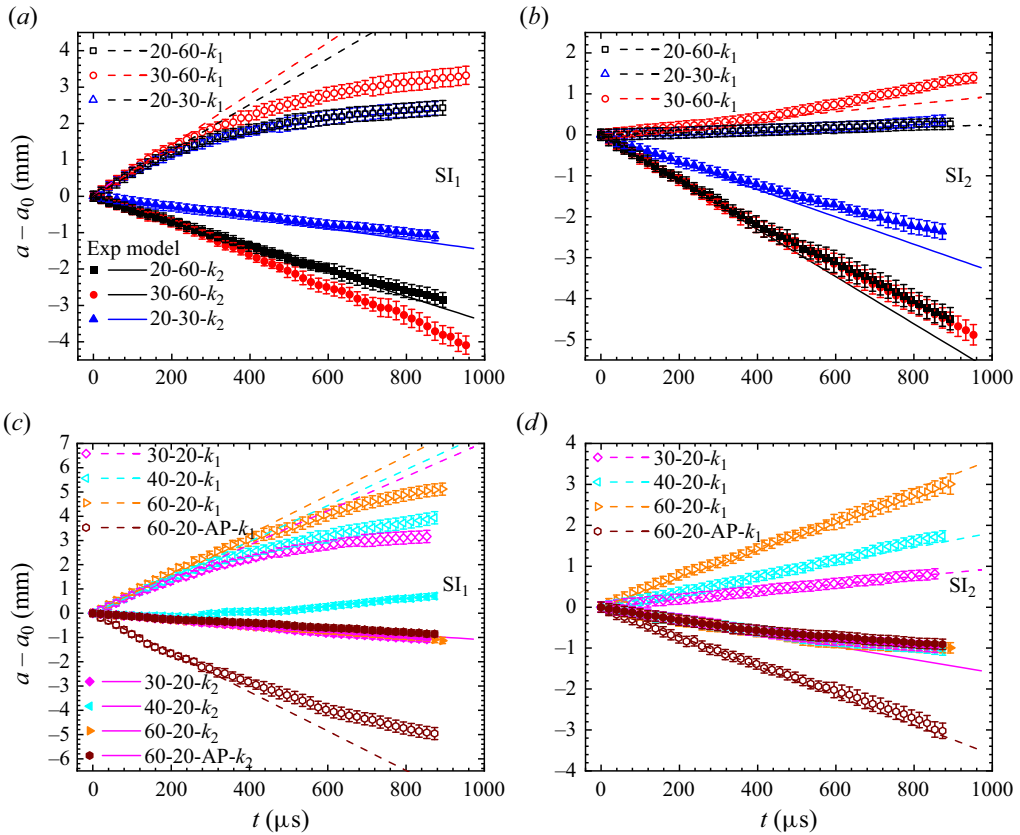
Figure 6. Comparisons of the amplitudes of k_1 and k_2 between experimental and theoretical results in cases (a,b) $K > 1$, and (c,d) $K < 1$. For the perturbations with the same wavelength, the predictions of the linear growth rate are the same, and only one theoretical line is provided. Here, the initial time is the moment when the linear growth of perturbation starts (after CW compress SI_2), and a_0 is the amplitude of the interface at the initial time, and similarly hereafter.

impacted by RW, and its amplitude (a_1^R) can be expressed as

$$a_1^R = \frac{(a_2^- + a_{RW})(R - 1)}{2}. \tag{3.19}$$

After perturbed RW collide with II_1, perturbed CW are formed, but are believed to recover to planar before they interact with SI_2 as mentioned before. The amplitude of SI_2 just before being impacted by CW (a_2^{C-}) differs significantly from a_2^+ (amplitude of SI_2 just after TS_1 impact) and can be expressed as

$$a_2^{C-} = a_2^- Z_2 + V_2^0(t_C - t_1), \tag{3.20}$$

where V_2^0 is the perturbation growth rate of SI_2 before being impacted by CW, and can be calculated by the MB model (Meyer & Blewett [1972]) as

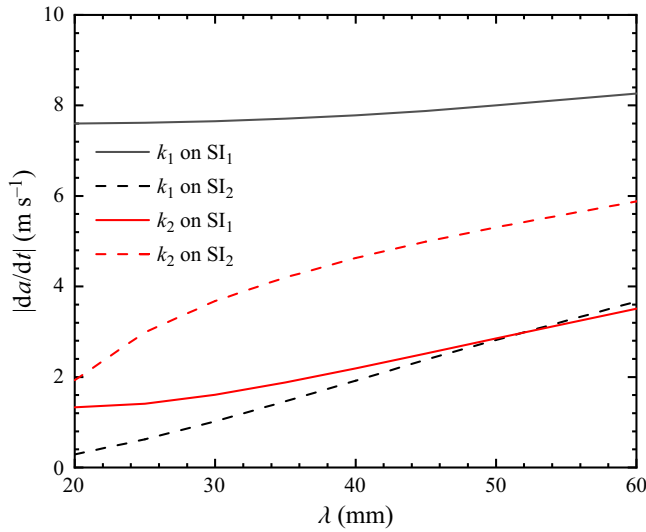$$V_2^0 = -k_2 a_2^0 A^+ \, \Delta u_2. \tag{3.21}$$

Figure 7. Dependence of linear growth rates of mode amplitudes, predicted by (3.16) and (3.25), on initial wavelength.

Then the average amplitude of SI_2 before and after being impacted by CW (a_2^C) is

$$a_2^C = a_2^{C-}(1 + Z_C)/2, \tag{3.22}$$

where $Z_C = (1 - \Delta u_C/c_2)$ is the compression factor of CW. Substituting a_1^+, a_2^0, a_1^R and a_2^C into (3.13), the linear growth rates of perturbations with k_2 on SI_1 and SI_2 can be predicted. However, the predictions deviate from the experimental results, which is probably ascribed to the assumption of deducing (3.11) that the velocity potentials of the flow in the layer are the same. Although the different accelerations of the two interfaces are considered, the effects of the disturbed RW and CW also need to be considered. In other words, when considering a planar II_1 and disturbed II_2 as shown in figure 5(*b*), SI_1 obtains a perturbation through both the waves' effect and interface coupling. Actually, the disturbed RW not only accelerates SI_1 but also obviously changes the perturbation growth. The impulsive model (Richtmyer 1960) is used to calculate the amplitude growth rate of SI_1 induced by the perturbed RW:

$$\frac{\mathrm{d}a_{1,R}}{\mathrm{d}t} = k_2 a_1^R \, \Delta u_R \, A^+. \tag{3.23}$$

When CW impacts SI_2, the amplitude of k_2 develops significantly and the MB model (Meyer & Blewett 1972) is used to predict the amplitude growth rate of SI_2 induced by CW:

$$\frac{\mathrm{d}a_{2,C}}{\mathrm{d}t} = -k_2 a_2^C \, \Delta u_C \, A^+. \tag{3.24}$$

Combining (3.13), (3.23) with (3.24), the model that can predict the linear growth rate of the perturbation with k_2 (the wavenumber of the initial second interface) on SI_1 and SI_2
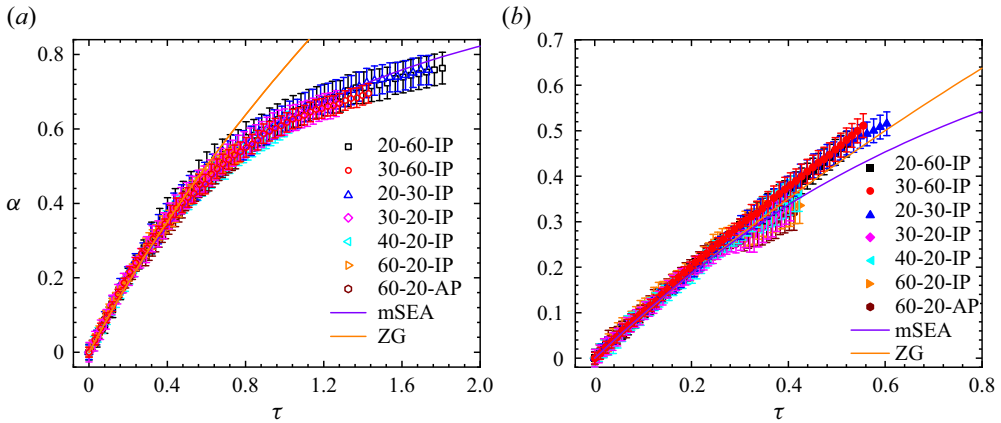
Figure 8. Comparison of the dimensionless amplitudes of the perturbation with (*a*) k_1 on SI_1 and (*b*) k_2 on SI_2.

can be written as

$$
\left.
\begin{aligned}
\frac{\mathrm{d}a_1}{\mathrm{d}t} &= \frac{k_2[A_t(\Delta u_R\, a_1^R - \Delta u_2\, a_2^0 - \Delta u_C\, a_2^C) + A_c(\Delta u_R\, a_1^R + \Delta u_2\, a_2^0 + \Delta u_C\, a_2^C)]}{2} \\
&\quad + k_2 a_1^R \Delta u_R A^+, \\
\frac{\mathrm{d}a_2}{\mathrm{d}t} &= \frac{k_2[A_t(\Delta u_R\, a_1^R - \Delta u_2\, a_2^0 - \Delta u_C\, a_2^C) - A_c(\Delta u_R\, a_1^R + \Delta u_2\, a_2^0 + \Delta u_C\, a_2^C)]}{2} \\
&\quad - k_2 a_2^C\, \Delta u_C A^+.
\end{aligned}
\right\}
\tag{3.25}
$$

The amplitude developments of k_2 on SI_1 and SI_2 are also presented in figure 6 for $K > 1$ (figures 6*a*,*b*) and $K < 1$ (figures 6*c*,*d*). On SI_2, the amplitude of k_2 grows first linearly and then nonlinearly. On SI_1, the linear model can well predict the amplitude growth of k_2. From figure 7, the linear growth rates of k_2 on both SI_1 and SI_2 are positively correlated with the wavelength of II_2 (λ_2). As a result, the linear growth rates of k_2 on both SI_1 and SI_2 are greater when λ_2 is larger. If the phases of two initial perturbations are opposite, then the linear models can also predict the growth rates of both k_1 and k_2.

3.2.3. *Nonlinear growth of amplitude*

As shown in figure 6, generally, only the amplitudes of k_1 (wavenumber of II_1) on SI_1, and k_2 (wavenumber of II_2) on SI_2, grow nonlinearly. The amplitude developments of perturbation with k_1 on SI_1 (k_2 on SI_2) in dimensionless form are shown in figure 8. On SI_1, the time and amplitude of k_1 are scaled as $\tau = k_1(\mathrm{d}a_1^l/\mathrm{d}t)t$ and $\alpha = k_1(a_1 - a_1^0)$, where $\mathrm{d}a_1^l/\mathrm{d}t$ is the experimental linear growth rate of k_1, and a_1^0 is the amplitude of k_1 at $t = 0$. On SI_2, the time and amplitude of k_2 are scaled as $\tau = k_2(\mathrm{d}a_2^l/\mathrm{d}t)t$ and $\alpha = k_2(a_2 - a_2^0)$, respectively, where $\mathrm{d}a_2^l/\mathrm{d}t$ is the experimental linear growth rate of k_2, and a_2^0 is the amplitude of k_2 at $t = 0$. The nonlinear amplitude growths of k_1 on SI_1 for cases collapse. However, for k_2 on SI_2, the amplitude growths in cases with $K > 1$ are different from those in cases with $K < 1$.

984 A38-14

Zhang & Guo (2016) previously proposed a nonlinear model (the ZG model) to predict the amplitude growth of a single interface. The ZG model can be described as

$$\frac{\mathrm{d}a_{b/s}^{ZG}}{\mathrm{d}t}(t) = \frac{\mathrm{d}a^l}{\mathrm{d}t} \frac{1}{1 + \theta k \dfrac{\mathrm{d}a^l}{\mathrm{d}t} t}, \tag{3.26}$$

where k is the wavenumber of the perturbation, $\mathrm{d}a^l/\mathrm{d}t$ is the linear growth rate of the perturbation after the waves impact, and

$$\theta = \frac{3}{4} \frac{(1+A^+)(3+A^+)}{3+A^+ + \sqrt{2(1+A^+)}} \times \frac{4(3+A^+) + \sqrt{2}(9+A^+)(1+A^+)^{1/2}}{(3+A^+)^2 + 2\sqrt{2}(3-A^+)(1+A^+)^{1/2}} \tag{3.27}$$

is a function for the Atwood number (A^+) of the shocked interface. The ZG model has been verified widely for a single-mode interface (Liu *et al.* 2018a; Guo *et al.* 2022), but it overestimates the nonlinear growth of k_1 on SI_1, as shown in figure 8(*a*). This indicates that in a heavy layer, interface coupling promotes nonlinearity of k_1 growth on SI_1, which is consistent with the observation in figure 3 that interface coupling greatly deforms the morphology of SI_1. For k_2 on SI_2, as shown in figure 8(*b*), the ZG model slightly overestimates the nonlinear amplitude growth for cases with $K < 1$, whereas it generally predicts the nonlinear amplitude growth for cases with $K > 1$. These indicate that interface coupling promotes nonlinearity of k_2 growth on SI_2 for cases with $K < 1$, but it has a little effect on the amplitude growth of k_2 on SI_2 for cases with $K > 1$. These conclusions are also consistent with the observations in figure 3.

The nonlinear model proposed by Sadot *et al.* (1998) (the SEA model) has been modified empirically (Dimonte & Ramaprabhu 2010; Mansoor *et al.* 2020) to predict the nonlinear growth of RM instability. The SEA model can be expressed as

$$\frac{\mathrm{d}a_{b/s}^{SEA}}{\mathrm{d}t}(t) = \frac{\mathrm{d}a^l}{\mathrm{d}t} \frac{1 + k \dfrac{\mathrm{d}a^l}{\mathrm{d}t} t}{1 + (1 \pm A^+)k \dfrac{\mathrm{d}a^l}{\mathrm{d}t} t + C(1 \pm A^+)/(1+A^+)\left(k\dfrac{\mathrm{d}a^l}{\mathrm{d}t}t\right)^2}, \tag{3.28}$$

where $C = 1$ for $|A| \to 0$, and $C = 1.5$ for $|A| > 0.5$. Based on the experimental results, the SEA model is modified empirically in the current work to predict the amplitude growths of two interfaces. The expression of the modified SEA model (mSEA model) can be described as

$$\frac{\mathrm{d}a_{b/s}^{mSEA}}{\mathrm{d}t}(t) = \frac{\mathrm{d}a^l}{\mathrm{d}t} \frac{1 + \dfrac{(1 \mp A^+)}{2}k \dfrac{\mathrm{d}a^l}{\mathrm{d}t} t}{1 + (1 \pm A^+)k \dfrac{\mathrm{d}a^l}{\mathrm{d}t} t + 5(1+A^+)(1-A^+)\left(k\dfrac{\mathrm{d}a^l}{\mathrm{d}t}t\right)^2}. \tag{3.29}$$

The predictions of the mSEA model for k_1 on SI_1 and k_2 on SI_2 are shown in figure 8. For k_2 on SI_2 in cases $K < 1$, and k_1 on SI_1, the mSEA model provides reasonable predictions.

3.2.4. *Modal evolution*

As described earlier, new modes are generated due to interface coupling on the interfaces except for the initial basic modes, then mode coupling arises. For the evolution of a

multi-mode interface, a modal model with second-order accuracy was proposed by Haan (1991) – referred to as the Haan model hereafter – to calculate the amplitude growth of the coupling modes resulting from the addition or subtraction of the initial basic modes. The Haan model was then simplified by Remington *et al.* (1994) with second-order accuracy to quantify mode coupling in the RT instability (denoted as the REM model) and modified by Luo *et al.* (2020) to predict the evolution of the multi-mode RM instability. However, all the previous models were solved and modified only for a single multi-mode interface but not for a gas layer. To quantify the mode-coupling effect in a shocked heavy layer, a new model is established by combining the REM model with (3.11)–(3.12). For the two different basic modes k_1 and k_2 on the initial interfaces considered in this work, the REM model (Remington *et al.* 1994) can be expressed as

$$a_{k_1 \pm k_2} = \mp \frac{1}{2}(k_1 \pm k_2)A^+(a_{k_1}^l a_{k_2}^l), \tag{3.30}$$

where a_{k_1} (a_{k_2}) is the amplitude of the perturbation with mode k_1 (k_2), $a_{k_1 \pm k_2}$ is the amplitude of the perturbation with coupling modes $k_1 \pm k_2$, and the superscript l denotes the linear regime. The right-hand side of (3.30) represents the generation of coupling mode $k_1 \pm k_2$ from initial modes k_1 and k_2. Taking the second derivative of (3.30) with time as in our previous work (Luo *et al.* 2020), one can obtain

$$\frac{\mathrm{d}^2 a_{k_1 \pm k_2}}{\mathrm{d}t^2} = \mp \frac{1}{2} A^+(k_1 \pm k_2) \left(\frac{\mathrm{d}^2 a_{k_1}^l}{\mathrm{d}t^2} a_{k_2}^l + \frac{\mathrm{d}^2 a_{k_2}^l}{\mathrm{d}t^2} a_{k_1}^l + 2 \frac{\mathrm{d}a_{k_1}^l}{\mathrm{d}t} \frac{\mathrm{d}a_{k_2}^l}{\mathrm{d}t} \right). \tag{3.31}$$

For a fluid layer, to quantify the evolution of $\mathrm{d}^2 a_{k_1}^l / \mathrm{d}t^2$ and $\mathrm{d}^2 a_{k_2}^l / \mathrm{d}t^2$, (3.11) can be written as follows: for the first interface,

$$\left.\begin{aligned}
\frac{\mathrm{d}^2 a_{1,k_1}^l}{\mathrm{d}t^2} &= \frac{k_1}{2} \left[A_{t,k_1}(g_1 a_{1,k_1}^l - g_2 a_{2,k_1}^l) + A_{c,k_1}(g_1 a_{1,k_1}^l + g_2 a_{2,k_1}^l) \right], \\
\frac{\mathrm{d}^2 a_{1,k_2}^l}{\mathrm{d}t^2} &= \frac{k_2}{2} \left[A_{t,k_2}(g_1 a_{1,k_2}^l - g_2 a_{2,k_2}^l) + A_{c,k_2}(g_1 a_{1,k_2}^l + g_2 a_{2,k_2}^l) \right];
\end{aligned}\right\} \tag{3.32}$$

for the second interface,

$$\left.\begin{aligned}
\frac{\mathrm{d}^2 a_{2,k_1}^l}{\mathrm{d}t^2} &= \frac{k_1}{2} \left[A_{t,k_1}(g_1 a_{1,k_1}^l - g_2 a_{2,k_1}^l) - A_{c,k_1}(g_1 a_{1,k_1}^l + g_2 a_{2,k_1}^l) \right], \\
\frac{\mathrm{d}^2 a_{2,k_2}^l}{\mathrm{d}t^2} &= \frac{k_2}{2} \left[A_{t,k_2}(g_1 a_{1,k_2}^l - g_2 a_{2,k_2}^l) - A_{c,k_2}(g_1 a_{1,k_2}^l + g_2 a_{2,k_2}^l) \right].
\end{aligned}\right\} \tag{3.33}$$

Substituting (3.32)–(3.33) into (3.31), the following expressions can be obtained: for the first interface,

$$\frac{\mathrm{d}^2 a_{1,k_1 \pm k_2}}{\mathrm{d}t^2} = \mp \frac{1}{2} A^+(|k_1 \pm k_2|)$$

$$\left\{ \frac{1}{2} \left[k_1 A_{t,k_1} \left(g_1 a_{1,k_1}^l - g_2 a_{2,k_1}^l \right) + k_1 A_{c,k_1}(g_1 a_{1,k_1}^l + g_2 a_{2,k_1}^l) \right] a_{1,k_2}^l \right.$$

$$+ \frac{1}{2} \left[k_2 A_{t,k_2}(g_1 a_{1,k_2}^l - g_2 a_{2,k_2}^l) + k_2 A_{c,k_2}(g_1 a_{1,k_2}^l + g_2 a_{2,k_2}^l) \right] a_{1,k_1}^l$$

$$\left. + 2 \frac{\mathrm{d}a_{1,k_1}^l}{\mathrm{d}t} \frac{\mathrm{d}a_{1,k_2}^l}{\mathrm{d}t} \right\}; \tag{3.34}$$

for the second interface,

$$
\frac{\mathrm{d}^2 a_{2,k_1 \pm k_2}}{\mathrm{d}t^2} = \mp \frac{1}{2} A^+ (|k_1 \pm k_2|)
$$

$$
\left\{ \frac{1}{2} \left[k_1 A_{t,k_1} (g_1 a_{1,k_1}^l - g_2 a_{2,k_1}^l) - k_1 A_{c,k_1} (g_1 a_{1,k_1}^l + g_2 a_{2,k_1}^l) \right] a_{2,k_2}^l \right.
$$

$$
+ \frac{1}{2} \left[k_2 A_{t,k_2} (g_1 a_{1,k_2}^l - g_2 a_{2,k_2}^l) - k_2 A_{c,k_2} (g_1 a_{1,k_2}^l + g_2 a_{2,k_2}^l) \right] a_{2,k_1}^l
$$

$$
\left. + 2 \frac{\mathrm{d}a_{2,k_1}^l}{\mathrm{d}t} \frac{\mathrm{d}a_{2,k_2}^l}{\mathrm{d}t} \right\}. \tag{3.35}
$$

Here, a_{1,k_1} (a_{2,k_1}), a_{1,k_2} (a_{2,k_2}) and $a_{1,k_1 \pm k_2}$ ($a_{2,k_1 \pm k_2}$) are the amplitudes of modes k_1, k_2 and $k_1 \pm k_2$ on SI$_1$ (SI$_2$), respectively; A_{t,k_1} (A_{t,k_2}) and A_{c,k_1} (A_{c,k_2}) are the two modified Atwood numbers of perturbation with k_1 (k_2), which can be expressed by (3.7), and g_1 (g_2) is the acceleration of the first (second) interface calculated by (3.12). Substituting g_1 and g_2 into (3.34)–(3.35) and then integrating (3.34)–(3.35), a model that can quantify the mode-coupling effect in a shocked layer is obtained and expressed as follows: for the first interface,

$$
\frac{\mathrm{d}a_{1,k_1 \pm k_2}}{\mathrm{d}t} = \mp \frac{1}{2} A^+ (|k_1 \pm k_2|)
$$

$$
\left\{ \frac{1}{2} \left[k_1 A_{t,k_1} \left(\Delta u_1 \, a_{1,k_1}^+ a_{1,k_2}^+ + \Delta u_R \, a_{1,k_1}^R a_{1,k_2}^R - \Delta u_2 \, a_{2,k_1}^0 a_{1,k_2}^+ - \Delta u_C \, a_{2,k_1}^C a_{1,k_2}^C \right) \right. \right.
$$

$$
\left. + k_1 A_{c,k_1} \left(\Delta u_1 \, a_{1,k_1}^+ a_{1,k_2}^+ + \Delta u_R \, a_{1,k_1}^R a_{1,k_2}^R + \Delta u_2 \, a_{2,k_1}^0 a_{1,k_2}^+ + \Delta u_C \, a_{2,k_1}^C a_{1,k_2}^C \right) \right]
$$

$$
+ \frac{1}{2} \left[k_2 A_{t,k_2} \left(\Delta u_1 \, a_{1,k_2}^+ a_{1,k_1}^+ + \Delta u_R \, a_{1,k_2}^R a_{1,k_1}^R - \Delta u_2 \, a_{2,k_2}^0 a_{1,k_1}^+ - \Delta u_C \, a_{2,k_2}^C a_{1,k_1}^C \right) \right.
$$

$$
\left. + k_2 A_{c,k_2} \left(\Delta u_1 \, a_{1,k_2}^+ a_{1,k_1}^+ + \Delta u_R \, a_{1,k_2}^R a_{1,k_1}^R + \Delta u_2 \, a_{2,k_2}^0 a_{1,k_1}^+ + \Delta u_C \, a_{2,k_2}^C a_{1,k_1}^C \right) \right]
$$

$$
\left. + 2 \int \frac{\mathrm{d}a_{1,k_1}^{mSEA}}{\mathrm{d}t} \frac{\mathrm{d}a_{1,k_2}^l}{\mathrm{d}t} \, \mathrm{d}t \right\}; \tag{3.36}
$$

for the second interface,

$$
\frac{\mathrm{d}a_{2,k_1 \pm k_2}}{\mathrm{d}t} = \mp \frac{1}{2} A^+ (|k_1 \pm k_2|)
$$

$$
\left\{ \frac{1}{2} \left[k_1 A_{t,k_1} \left(\Delta u_1 \, a_{1,k_1}^+ a_{2,k_2}^0 + \Delta u_R \, a_{1,k_1}^R a_{2,k_2}^R - \Delta u_2 \, a_{2,k_1}^0 a_{2,k_2}^0 - \Delta u_C \, a_{2,k_1}^C a_{2,k_2}^C \right) \right. \right.
$$

$$
\left. - k_1 A_{c,k_1} \left(\Delta u_1 \, a_{1,k_1}^+ a_{2,k_2}^0 + \Delta u_R \, a_{1,k_1}^R a_{2,k_2}^R + \Delta u_2 \, a_{2,k_1}^0 a_{2,k_2}^0 + \Delta u_C \, a_{2,k_1}^C a_{2,k_2}^C \right) \right]
$$

$$
+ \frac{1}{2} \left[k_2 A_{t,k_2} \left(\Delta u_1 \, a_{1,k_2}^+ a_{2,k_1}^0 + \Delta u_R \, a_{1,k_2}^R a_{2,k_1}^R - \Delta u_2 \, a_{2,k_2}^0 a_{2,k_1}^0 - \Delta u_C \, a_{2,k_2}^C a_{2,k_1}^C \right) \right.
$$

$$
\left. - k_2 A_{c,k_2} \left(\Delta u_1 \, a_{1,k_2}^+ a_{2,k_1}^0 + \Delta u_R \, a_{1,k_2}^R a_{2,k_1}^R + \Delta u_2 \, a_{2,k_2}^0 a_{2,k_1}^0 + \Delta u_C \, a_{2,k_2}^C a_{2,k_1}^C \right) \right]
$$

$$
\left. + 2 \int \frac{\mathrm{d}a_{2,k_1}^l}{\mathrm{d}t} \frac{\mathrm{d}a_{2,k_2}^{ZG}}{\mathrm{d}t} \, \mathrm{d}t \right\}. \tag{3.37}
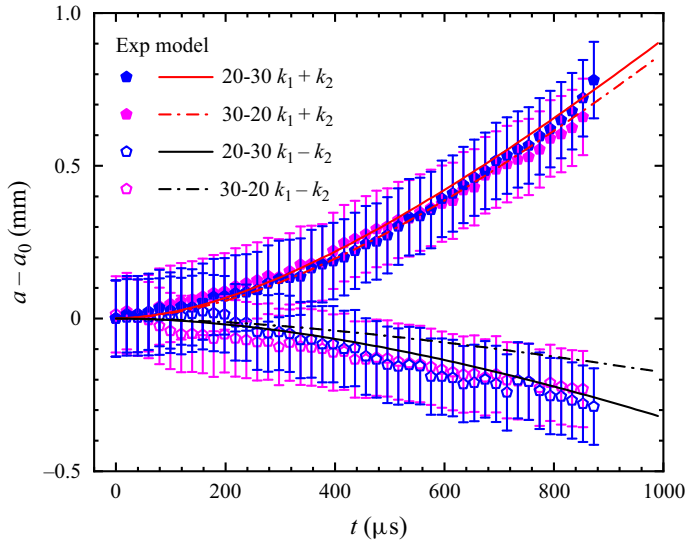$$

Figure 9. Comparison of the developments of $a_{1,k_1\pm k_2}$ between experimental measurements and theoretical predictions in cases 20-30-IP and 30-20-IP.

Here, a_1^+ (a_1^R) represents the amplitude of the first interface just being impacted by IS (RW), and a_2^0 (a_2^C) is the average amplitude of the second interface before and after being impacted by TS$_1$ (CW), as defined before. In this work, a_{1,k_2}^+, a_{2,k_1}^0, a_{2,k_1}^R and a_{2,k_1}^C are all equal to zero, and other specific amplitudes can be calculated through the linear theory mentioned in §3.2.2. In the integral terms on the right-hand sides of (3.34) and (3.35), $\mathrm{d}a_{1,k_2}^l/\mathrm{d}t$ and $\mathrm{d}a_{2,k_1}^l/\mathrm{d}t$ can be calculated by (3.16) and (3.25), but $\mathrm{d}a_{1,k_1}^l/\mathrm{d}t$ and $\mathrm{d}a_{2,k_2}^l/\mathrm{d}t$ are substituted respectively with $\mathrm{d}a_{1,k_1}^{mSEA}/\mathrm{d}t$ expressed in (3.29) and $\mathrm{d}a_{2,k_2}^{ZG}/\mathrm{d}t$ expressed in (3.26), because the growths of a_{1,k_1} and a_{2,k_2} quickly enter the nonlinear stage.

For cases 20-30-IP and 30-20-IP, modes $k_1 \pm k_2$ and harmonics have no influence on the growths of a_{2,k_1} and a_{1,k_2}. As a result, the linear models can provide accurate predictions for these two amplitude developments. From figure 3, a nearly perfect single-mode profile of SI$_2$ is observed in case 20-30-IP, which means that mode coupling on SI$_2$ is very weak, i.e. $a_{2,k_1\pm k_2}$ should be very small and the predictions are ignored. Besides, $a_{2,k_1\pm k_2}$ in case 30-20-IP are also very limited. Therefore, only the developments of $a_{1,k_1\pm k_2}$ in these two cases are predicted by (3.36) and discussed here. As presented in figure 9, the theories provide good predictions for the amplitude developments of these coupling modes. Note that the deviation between experiment and theoretical model for the developments of a_{1,k_1-k_2} for the 30-20 case seems significant, which is caused mainly by the relatively small range of the vertical axis in figure 9. Considering the error bars, the model can reasonably predict the experimental results for a_{1,k_1-k_2}.

For cases 60-20-IP (20-60-IP) and 60-20-AP, the coupling mode $k_2 - k_1$ ($k_1 - k_2$) can be described as the second-order harmonic of k_1 (k_2). For case 40-20-IP (30-60-IP), $k_2 = 2k_1$ ($k_1 = 2k_2$). To fully quantify the modal evolutions, the amplitude growths of the harmonics are also considered after constructing (3.36) and (3.37) for $k_1 \pm k_2$. Based on the perturbation expansion method, the ZS model was proposed (Zhang & Sohn 1997) to calculate the amplitude growth of the harmonics for a single-mode interface. Here, the ZS model is considered for the amplitude growth of the second-order harmonics: for the

first interface,

$$
\left.\begin{aligned}
a_{1,2k_1} &= \frac{1}{2}A^+ k_1 \frac{\mathrm{d}a^l_{1,k_1}}{\mathrm{d}t} t^2 - \frac{1}{12}k_1^3 \left(\frac{\mathrm{d}a^l_{1,k_1}}{\mathrm{d}t}\right)^2 \left[4(A^+)^3 \left(\frac{\mathrm{d}a^l_{1,k_1}}{\mathrm{d}t}\right)^2 t^4 + 3A^+ a^R_{1,k_1} t^2\right], \\
a_{1,2k_2} &= \frac{1}{2}A^+ k_2 \frac{\mathrm{d}a^l_{1,k_2}}{\mathrm{d}t} t^2 - \frac{1}{12}k_2^3 \left(\frac{\mathrm{d}a^l_{1,k_2}}{\mathrm{d}t}\right)^2 \left[4(A^+)^3 \left(\frac{\mathrm{d}a^l_{1,k_2}}{\mathrm{d}t}\right)^2 t^4 + 3A^+ a^R_{1,k_2} t^2\right];
\end{aligned}\right\}
$$

$$(3.38)$$

for the second interface,

$$
\left.\begin{aligned}
a_{2,2k_1} &= \frac{1}{2}A^+ k_1 \frac{\mathrm{d}a^l_{2,k_1}}{\mathrm{d}t} t^2 - \frac{1}{12}k_1^3 \left(\frac{\mathrm{d}a^l_{2,k_1}}{\mathrm{d}t}\right)^2 \left[4(A^+)^3 \left(\frac{\mathrm{d}a^l_{2,k_1}}{\mathrm{d}t}\right)^2 t^4 + 3A^+ a^C_{2,k_1} t^2\right], \\
a_{2,2k_2} &= \frac{1}{2}A^+ k_2 \frac{\mathrm{d}a^l_{2,k_2}}{\mathrm{d}t} t^2 - \frac{1}{12}k_2^3 \left(\frac{\mathrm{d}a^l_{2,k_2}}{\mathrm{d}t}\right)^2 \left[4(A^+)^3 \left(\frac{\mathrm{d}a^l_{2,k_2}}{\mathrm{d}t}\right)^2 t^4 + 3A^+ a^C_{2,k_2} t^2\right].
\end{aligned}\right\}
$$

$$(3.39)$$

For the single-mode RM instability, previous work (Liu *et al.* 2018*a*) has shown that the amplitudes of harmonics higher than third order grow slowly and can be ignored. Therefore, only the second-order harmonic is considered in this work. The linear and nonlinear developments of amplitudes of the basic modes (a_{1,k_1} and a_{2,k_2}) can be well predicted through (3.16), (3.25), (3.26) and (3.29). Considering the amplitudes of other modes, (3.36)–(3.39) are used to provide predictions for modal evolutions.

For cases 20-60-IP, 60-20-IP and 60-20-AP, the linear models can also well predict the growths of a_{1,k_2} and a_{2,k_1}. The experimental amplitudes of mode $k_1 + k_2$ agree with the predictions by (3.36)–(3.37), as given in figures 10(*a,b*). However, for predicting the amplitude of mode $|k_1 - k_2|$, the effect of harmonics needs to be considered because $|k_1 - k_2| = 2k_1$ or $2k_2$. Through adding (3.38)–(3.39) to (3.36)–(3.37), the amplitude growths of $|k_1 - k_2|$ can be well predicted. For cases 30-60-IP and 40-20-IP, because $k_1 = 2k_2$ and $k_2 = 2k_1$, the second-order harmonics and mode-coupling mode ($|k_1 - k_2|$) directly affect the growth of a_{2,k_1} and a_{1,k_2}, therefore the linear models fail to predict the growths of a_{1,k_2} and a_{2,k_1} at late stages. Combining (3.16), (3.25) with (3.36)–(3.39), the predictions for a_{1,k_2} and a_{2,k_1} in these two cases are provided. In case 40-20-IP, the amplitude growth of k_2 on SI$_1$ even experiences a phase inversion process because the harmonic induced by k_1 develops faster than the linear growth of k_2 at late stages. To predict the developments of $a_{1,k_1 \pm k_2}$ and $a_{2,k_1 \pm k_2}$, (3.36)–(3.37) are adopted and $\mathrm{d}a^l_{1,k_2}/\mathrm{d}t$ ($\mathrm{d}a^l_{2,k_1}/\mathrm{d}t$) is replaced with $\mathrm{d}a_{1,k_2}/\mathrm{d}t$ ($\mathrm{d}a_{2,k_1}/\mathrm{d}t$), which is calculated by combining the linear model with the mode-coupling model and harmonic model.

In summary, through combining the linear models (3.16) and (3.25), and nonlinear models (3.26) and (3.29), with modal models (3.36)–(3.39), a complete theory that can reasonably predict the amplitude growths of the basic modes (a_{1,k_1} and a_{2,k_2}), the modes generated by interface coupling (a_{2,k_1} and a_{1,k_2}), and the modes generated by mode coupling ($a_{k_1 \pm k_2}$) is established. By comparing the results in figures 6 and 10, we see that mode coupling is significant (ignorable) for the growth of a_{2,k_1} and a_{1,k_2} (a_{1,k_1} and a_{2,k_2}).
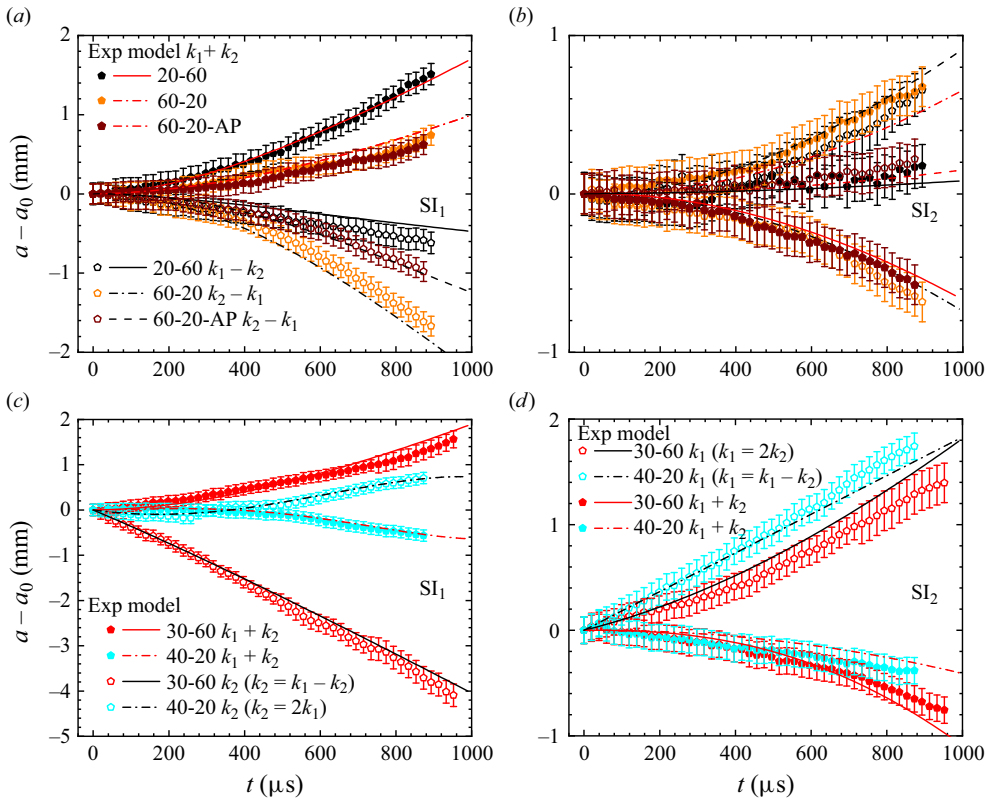
Figure 10. Comparisons of the amplitudes of $k_1 \pm k_2$ measured from experiments with models in (a,b) cases 20-60, 60-20 and 60-20-AP, and (c,d) cases 30-60 and 40-20.

3.2.5. *Freeze-out of the second interface growth*

In previous work, freeze-out of amplitude growth (i.e. the amplitude growth stagnates) was realized by compressibility (Mikaelian 1994), the second successive shock impact (Charakhch'yan 2001) or the weak reflected shock/rarefaction wave impact (Chen *et al.* 2023*a,b*). In this work, if the first interface is planar and the second interface is single-mode, then amplitude freeze-out of the second interface may be realized through interface coupling according to (3.25). In other words, amplitude freeze-out of a single-mode heavy–light perturbation could be realized through interface coupling by adding a planar light–heavy interface in front of the perturbed interface. Evidently, the condition for the amplitude freeze-out of the second interface is $da_2/dt = 0$, i.e.

$$
\begin{aligned}
0 = \frac{1}{2} \Bigg\{ & A_t \left(\Delta u_R \, \frac{1 + Z_2 + k_2 c_1 u_r (t_R - t_1)}{2} \, (R - 1) - \Delta u_2 \, \frac{1 + Z_2}{2} \right. \\
& - \Delta u_C \left(Z_2 - k_2 \, \frac{1 + Z_2}{2} \, A^+ \, \Delta u_2 \, (t_C - t_1) \right) (1 + Z_C)/2 \Bigg) \\
& - A_c \left(\Delta u_R \, \frac{1 + Z_2 + k_2 c_1 u_r (t_R - t_1)}{2} \, (R - 1) + \Delta u_2 \, \frac{1 + Z_2}{2} \right.
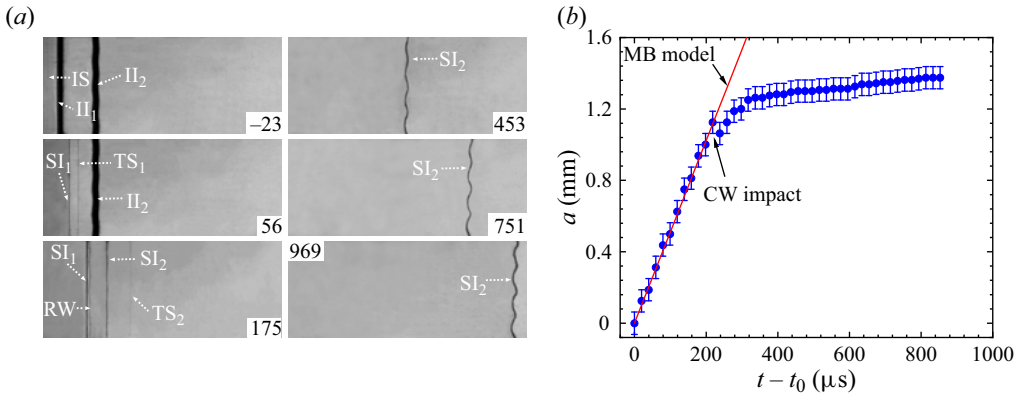\end{aligned}
$$

Figure 11. (*a*) Schlieren images showing the evolution of the SF$_6$–air interface. (*b*) The temporal variations of the amplitude of SI$_2$ after the phase inversion is finished at $t = t_0$.

$$
+ \Delta u_C \left(Z_2 - k_2 \frac{1 + Z_2}{2} A^+ \Delta u_2 \left(t_C - t_1\right) \right) (1 + Z_C)/2 \bigg) \Bigg\}
$$
$$
- \Delta u_C A^+ \left(Z_2 - k_2 \frac{1 + Z_2}{2} A^+ \Delta u_2 \left(t_C - t_1\right) \right) (1 + Z_C)/2. \tag{3.40}
$$

Here, all the parameters except k_2 are dependent on the shock intensity, gas properties and L_0, but are independent of the initial amplitude. Based on (3.40), when the shock intensities and gas properties are fixed, k_2 and L_0 satisfy the specific relationship to achieve the amplitude freeze-out of the second interface. According to this relationship, an experiment with $k_2 = 20$ mm, $k_2 a_2^- = 0.083$ and $L_0 = 27$ mm is designed and conducted. The shock intensity and gas properties are the same as the other cases in this work. The typical schlieren images of the perturbed SF$_6$–air interface are provided in figure 11(*a*), in which SI$_1$ is not shown after 453 μs. After CW impacts SI$_2$ (453–969 μs), the amplitude of SI$_2$ changes very slowly, and amplitude freeze-out is almost achieved. Note that if the first interface is perturbed and the second interface is planar, then it is impossible to achieve the amplitude freeze-out of the first interface through changing L_0 based on (3.16).

The amplitude development of the second interface after the phase inversion is shown in figure 11(*b*), in which t_0 is the time when the phase inversion is completed. The amplitude of SI$_2$ grows linearly and can be well predicted by the MB model before CW arrive. This also proves that when II$_1$ is planar, interface coupling does not affect the perturbation evolution on SI$_2$ before CW impact. After CW impact SI$_2$, the amplitude is compressed first and then rises for a short while because interface coupling needs a start-up process. When the start-up process is finished, the amplitude almost settles in a steady-state value, and freeze-out is almost realized (the tiny increase of the amplitude may be attributed to the negligible error of the theory). As a result, amplitude freeze-out of a single-mode SF$_6$–air interface is almost realized experimentally through generating a planar air–SF$_6$ interface upstream with a suitable distance.

Through interface coupling between two successive heavy–light interfaces, the amplitude freeze-out of a heavy–light interface was realized numerically by Liang & Luo (2023*a*). However, the initial amplitudes of two successive interfaces need to satisfy a specific relationship that is difficult to realize in ICF. In the present work, the first light–heavy interface is planar, and amplitude freeze-out of the second

perturbed heavy–light interface is achieved just by simply manipulating the distance of two interfaces. In previous work for the target designs in ICF (Qiao & Lan 2021), the glow discharge polymer plastic (CH, with density $1.05\,\mathrm{g\,cm^{-3}}$) was used as the outermost ablator layer, while the high-density carbon (HDC, with density $3.48\,\mathrm{g\,cm^{-3}}$) was kept as the main ablator. Through constructing the outer CH-HDC interface, the hydrodynamic instabilities on the interface between HDC and the deuterium–tritium ice (DT ice, with density $0.26\,\mathrm{g\,cm^{-3}}$) can be reduced significantly. The CH-HDC interface (light–heavy) and the HDC-DT interface (heavy–light) construct a heavy layer. The decreasing instabilities on the inner HDC-DT interface coincide with the finding in this work that the amplitude freeze-out of the second interface can be realized in a shocked heavy layer. These findings suggest that in ICF, through generating a light–heavy interface with a suitable distance upstream from the interface separating the ablator material and DT ice, the RM instability may be effectively suppressed.

4. Conclusions

We performed the shock-tube experiments and theoretical studies to highlight mode coupling between two single-mode interfaces with different basic modes. Experimentally, the soap-film technique is used to create planar and single-mode interfaces of the layers. Experimental results are presented and analysed for an initially undisturbed layer, and the seven different kinds of disturbed layers. The schlieren images clearly show the interface morphologies, and the distinct profiles facilitate the modal analysis.

The results indicate that the rarefaction waves (RW) and compression waves (CW) generated in the layer, respectively, accelerate the first and second interface movements. Generally, after CW impact, both interfaces move steadily, which means that the effects of other waves can be ignored. For the perturbed layers, just after CW impact, the perturbations on two interfaces still present single-mode shapes with the basic modes. As two interfaces become closer, interface coupling induces a different mode from the basic mode on each interface. Then mode coupling further generates new modes and complicates the interface profile. The interface with a smaller initial wavenumber generally remains a quasi-single-mode profile, and the bubbles (spikes) develop symmetrically. The multi-mode features become prominent on the interface with a larger initial wavenumber, and the bubbles (spikes) grow with an inclination and size difference.

In the linear regime, the mode-coupling effect is weak, and the linear growth of the basic mode is considered separately. The linear model proposed by Jacobs *et al.* (1995) is modified by considering the different accelerations of two interfaces and the waves' effects in the layer. The modified linear model provides good predictions to the linear growth rates of the basic modes and the modes generated by interface coupling. In the nonlinear regime, the amplitude growths of the basic modes can be characterized generally by the existing or modified nonlinear model. It is found that interface coupling promotes nonlinearity of the basic mode growth on the first interface, but behaves differently to the nonlinear growth of the basic mode on the second interface. Moreover, a new modal model is established based on the model proposed by Remington *et al.* (1994) to quantify the mode-coupling effect in a gas layer. Besides, the model proposed by Zhang & Sohn (1997) (the ZS model) with fourth-order accuracy is used to characterize the growth of second-order harmonics. Combining the linear model, new modal model with the ZS model, the amplitude growths of modes generated by both mode coupling and interface coupling are well predicted. The mode-coupling effect on the amplitude growth is negligible for the basic modes, but is

significant for the interface-coupling modes when the initial one wavenumber is twice the other wavenumber.

The present studies show that if a planar light–heavy interface is added in front of the single-mode heavy–light interface, then amplitude freeze-out of the heavy–light interface is possible, caused by interface coupling. Theoretically, the conditions for amplitude freeze-out of the second single-mode interface are independent of initial amplitude but dependent on initial wavelength and width of the layer. According to the predictions of initial conditions, the specific experiment is designed and conducted. It is verified that amplitude freeze-out of the second interface can be realized after CW impact. These findings suggest that in ICF, through generating a planar light–heavy interface with a suitable distance upstream from the interface separating the ablator material and deuterium–tritium ice, the hydrodynamic instabilities may be suppressed effectively.

Declaration of interests. The authors report no conflict of interest.

Author ORCIDs.

He Wang https://orcid.org/0000-0002-6497-6673;

Zhigang Zhai https://orcid.org/0000-0002-0094-5210;

Xisheng Luo https://orcid.org/0000-0002-4303-8290.

REFERENCES

BETTI, R. & HURRICANE, O.A. 2016 Inertial-confinement fusion with lasers. *Nat. Phys.* **12**, 435–448.

BROUILLETTE, M. 2002 The Richtmyer–Meshkov instability. *Annu. Rev. Fluid Mech.* **34**, 445–468.

CHARAKHCH'YAN, A.A. 2001 Reshocking at the non-linear stage of Richtmyer–Meshkov instability. *Plasma Phys. Control. Fusion* **43**, 1169–1179.

CHEN, C., WANG, H., ZHAI, Z. & LUO, X. 2023*a* Attenuation of perturbation growth of single-mode SF_6–air interface through reflected rarefaction waves. *J. Fluid Mech.* **969**, R1.

CHEN, C., XING, Y., WANG, H., ZHAI, Z. & LUO, X. 2023*b* Freeze-out of perturbation growth of single-mode helium–air interface through reflected shock in Richtmyer–Meshkov flows. *J. Fluid Mech.* **956**, R2.

DI STEFANO, C., MALAMUD, G., KURANZ, C., KLEIN, S., STOECKL, C. & DRAKE, R. 2015 Richtmyer–Meshkov evolution under steady shock conditions in the high-energy-density regime. *Appl. Phys. Lett.* **106**, 114103.

DIMONTE, G. & RAMAPRABHU, P. 2010 Simulations and model of the nonlinear Richtmyer–Meshkov instability. *Phys. Fluids* **22**, 014104.

GUO, X., CONG, Z., SI, T. & LUO, X. 2022 Shock-tube studies of single- and quasi-single-mode perturbation growth in Richtmyer–Meshkov flows with reshock. *J. Fluid Mech.* **941**, A65.

HAAN, S.W. 1991 Weakly nonlinear hydrodynamic instabilities in inertial fusion. *Phys. Fluids* B **3**, 2349–2355.

ISHIZAKI, R. & NISHIHARA, K. 1997 Propagation of a rippled shock wave driven by nonuniform laser ablation. *Phys. Rev. Lett.* **78**, 1920–1923.

JACOBS, J., JENKINS, D., KLEIN, D. & BENJAMIN, R. 1995 Nonlinear growth of the shock-accelerated instability of a thin fluid layer. *J. Fluid Mech.* **295**, 23–42.

JACOBS, J., KLEIN, D., JENKINS, D. & BENJAMIN, R. 1993 Instability growth patterns of a shock-accelerated thin fluid layer. *Phys. Rev. Lett.* **70**, 583–586.

KURANZ, C., *et al.* 2018 How high energy fluxes may affect Rayleigh–Taylor instability growth in young supernova remnants. *Nat. Commun.* **9**, 1564.

LIANG, Y. 2022 The phase effect on the Richtmyer–Meshkov instability of a fluid layer. *Phys. Fluids* **34**, 034106.

LIANG, Y., LIU, L., ZHAI, Z., DING, J., SI, T. & LUO, X. 2021 Richtmyer–Meshkov instability on two-dimensional multi-mode interfaces. *J. Fluid Mech.* **928**, A37.

LIANG, Y. & LUO, X. 2021 On shock-induced heavy-fluid-layer evolution. *J. Fluid Mech.* **920**, A13.

LIANG, Y. & LUO, X. 2023*a* Hydrodynamic instabilities of two successive slow/fast interfaces induced by a weak shock. *J. Fluid Mech.* **955**, A40.

LIANG, Y. & LUO, X. 2023*b* Review on hydrodynamic instabilities of a shocked gas layer. *Sci. China-Phys. Mech. Astron.* **66**, 104701.

LINDL, J., LANDEN, O., EDWARDS, J., MOSES, E. & TEAM, N. 2014 Review of the national ignition campaign 2009–2012. *Phys. Plasmas* **21**, 020501.

LIU, L., LIANG, Y., DING, J., LIU, N. & LUO, X. 2018*a* An elaborate experiment on the single-mode Richtmyer–Meshkov instability. *J. Fluid Mech.* **853**, R2.

LIU, W., LI, X., YU, C., FU, Y., WANG, P., WANG, L. & YE, W. 2018*b* Theoretical study on finite-thickness effect on harmonics in Richtmyer–Meshkov instability for arbitrary Atwood numbers. *Phys. Plasmas* **25**, 122103.

LUO, X., LIU, L., LIANG, Y., DING, J. & WEN, C. 2020 Richtmyer–Meshkov instability on a dual-mode interface. *J. Fluid Mech.* **905**, A5.

MANSOOR, M.M., DALTON, S.M., MARTINEZ, A.A., DESJARDINS, T., CHARONKO, J.J. & PRESTRIDGE, K.P. 2020 The effect of initial conditions on mixing transition of the Richtmyer–Meshkov instability. *J. Fluid Mech.* **904**, A3.

MCFARLAND, J., REILLY, D., BLACK, W., GREENOUGH, J. & RANJAN, D. 2015 Modal interactions between a large-wavelength inclined interface and small-wavelength multimode perturbations in a Richtmyer–Meshkov instability. *Phys. Rev.* E **92**, 013023.

MESHKOV, E.E. 1969 Instability of the interface of two gases accelerated by a shock wave. *Fluid Dyn.* **4**, 101–104.

MEYER, K.A. & BLEWETT, P.J. 1972 Numerical investigation of the stability of a shock-accelerated interface between two fluids. *Phys. Fluids* **15**, 753–759.

MIKAELIAN, K.O. 1985 Richtmyer–Meshkov instabilities in stratified fluids. *Phys. Rev.* A **31**, 410–419.

MIKAELIAN, K.O. 1994 Freeze-out and the effect of compressibility in the Richtmyer–Meshkov instability. *Phys. Fluids* **6**, 356–368.

MIKAELIAN, K.O. 1995 Rayleigh–Taylor and Richtmyer–Meshkov instabilities in finite-thickness fluid layers. *Phys. Fluids* **7**, 888–890.

MIKAELIAN, K.O. 1996 Numerical simulations of Richtmyer–Meshkov instabilities in finite-thickness fluid layers. *Phys. Fluids* **8**, 1269–1292.

MOHAGHAR, M., CARTER, J., PATHIKONDA, G. & RANJAN, D. 2019 The transition to turbulence in shock-driven mixing: effects of Mach number and initial conditions. *J. Fluid Mech.* **871**, 595–635.

OFER, D., ALON, U., SHVARTS, D., MCCRORY, R. & VERDON, C. 1996 Modal model for the nonlinear multimode Rayleigh–Taylor instability. *Phys. Plasmas* **3**, 3073–3090.

PRESTRIDGE, K., VOROBIEFF, P., RIGHTLEY, P. & BENJAMIN, R. 2000 Validation of an instability growth model using particle image velocimetry measurements. *Phys. Rev. Lett.* **84**, 4353–4356.

QIAO, X. & LAN, K. 2021 Novel target designs to mitigate hydrodynamic instabilities growth in inertial confinement fusion. *Phys. Rev. Lett.* **126**, 185001.

RANJAN, D., OAKLEY, J. & BONAZZA, R. 2011 Shock–bubble interactions. *Annu. Rev. Fluid Mech.* **43**, 117–140.

RAYLEIGH, LORD 1883 Investigation of the character of the equilibrium of an incompressible heavy fluid of variable density. *Proc. Lond. Math. Soc.* **14**, 170–177.

REMINGTON, B., WEBER, S., MARINAK, M., HAAR, S., KILKENNY, J., WALLACE, R. & DIMONTE, G. 1994 Multimode Rayleigh–Taylor experiments on Nova. *Phys. Rev. Lett.* **73**, 545–548.

RICHTMYER, R.D. 1960 Taylor instability in shock acceleration of compressible fluids. *Commun. Pure Appl. Maths* **13**, 297–319.

RIKANATI, A., ALON, U. & SHVARTS, D. 1998 Vortex model for the nonlinear evolution of the multimode Richtmyer–Meshkov instability at low Atwood numbers. *Phys. Rev.* E **58**, 7410–7418.

RIKANATI, A., ORON, D., SADOT, O. & SHVARTS, D. 2003 High initial amplitude and high Mach number effects on the evolution of the single-mode Richtmyer–Meshkov instability. *Phys. Rev.* E **67**, 026307.

SADOT, O., EREZ, L., ALON, U., ORON, D., LEVIN, L.A., EREZ, G., BEN-DOR, G. & SHVARTS, D. 1998 Study of nonlinear evolution of single-mode and two-bubble interaction under Richtmyer–Meshkov instability. *Phys. Rev. Lett.* **80**, 1654–1657.

TAYLOR, G. 1950 The instability of liquid surfaces when accelerated in a direction perpendicular to their planes. I. *Proc. R. Soc. Lond.* A **201**, 192–196.

VANDENBOOMGAERDE, M., GAUTHIER, S. & MÜGLER, C. 2002 Nonlinear regime of a multimode Richtmyer–Meshkov instability: a simplified perturbation theory. *Phys. Fluids* **14**, 1111–1122.

VELIKOVICH, A. & PHILLIPS, L. 1996 Instability of a plane centered rarefaction wave. *Phys. Fluids* **8**, 1107–1118.

WANG, H., CAO, Q., CHEN, C., ZHAI, Z. & LUO, X. 2022 Experimental study on a light–heavy interface evolution induced by two successive shock waves. *J. Fluid Mech.* **953**, A15.

WANG, H., WANG, H., ZHAI, Z. & LUO, X. 2023 High-amplitude effect on single-mode Richtmyer–Meshkov instability of a light–heavy interface. *Phys. Fluids* **35**, 016106.

XU, J., WANG, H., ZHAI, Z. & LUO, X. 2023 Convergent Richtmyer–Meshkov instability on two-dimensional dual-mode interfaces. *J. Fluid Mech.* **965**, A8.

YANG, J., KUBOTA, T. & ZUKOSKI, E. 1993 Applications of shock-induced mixing to supersonic combustion. *AIAA J.* **31**, 854–862.

ZABUSKY, N.J. 1999 Vortex paradigm for accelerated inhomogeneous flows: visiometrics for the Rayleigh–Taylor and Richtmyer–Meshkov environments. *Annu. Rev. Fluid Mech.* **31**, 495–536.

ZHAI, Z., ZOU, L., WU, Q. & LUO, X. 2018 Review of experimental Richtmyer–Meshkov instability in shock tube: from simple to complex. *Proc. Inst. Mech. Engng* C **232**, 2830–2849.

ZHANG, D., DING, J., SI, T. & LUO, X. 2023 Divergent Richtmyer–Meshkov instability on a heavy gas layer. *J. Fluid Mech.* **959**, A37.

ZHANG, Q. & GUO, W. 2016 Universality of finger growth in two-dimensional Rayleigh–Taylor and Richtmyer–Meshkov instabilities with all density ratios. *J. Fluid Mech.* **786**, 47–61.

ZHANG, Q. & SOHN, S.I. 1997 Nonlinear theory of unstable fluid mixing driven by shock wave. *Phys. Fluids* **9**, 1106–1124.

ZHOU, Y. 2017a Rayleigh–Taylor and Richtmyer–Meshkov instability induced flow, turbulence, and mixing. I. *Phys. Rep.* **720–722**, 1–136.

ZHOU, Y. 2017b Rayleigh–Taylor and Richtmyer–Meshkov instability induced flow, turbulence, and mixing. II. *Phys. Rep.* **723–725**, 1–160.

ZHOU, Y., *et al.* 2021 Rayleigh–Taylor and Richtmyer–Meshkov instabilities: a journey through scales. *Physica D* **423**, 132838.